CFD analysis of cooling effects in H$_2$-fed solid oxide fuel cells

M. García-Camprubí[a], H. Jasak[b], N. Fueyo[a,*]

[a] Fluid Mechanics Group (University of Zaragoza) and LITEC (CSIC), Spain
[b] Faculty of Mechanical Engineering and Naval Architecture, University of Zagreb, Croatia

ARTICLE INFO

ABSTRACT

A model is presented that describes the main physical phenomena affecting in the performance of a Solid-Oxide Fuel Cell (SOFC). The implementation of the model uses an in-house algorithm in a computational fluid-dynamics (CFD) framework that may be used to optimize the SOFC operational parameters. The physical phenomena considered in the model are: (i) mass conservation: multicomponent and multi-modal mass transfer in gas channels and electrodes (convection, ordinary diffusion, Knudsen diffusion); (ii) momentum conservation in the gas channels and electrodes; (iii) energy conservation: coupled heat transfer across the whole cell (gas channels, electrodes and electrolyte); (iv) electrochemistry: half-reactions are considered to take place at the electrode–electrolyte interfaces, and activation losses are computed using the general version of the Butler-Volmer equation. The main features of this CFD tool are: (i) it allows the prediction of the characteristic (I–V) curve of an H$_2$-fed cell; (ii) it is suitable for both tubular and planar cells; (iii) it has been implemented using OpenFOAM-1.5-dev, an open-source CFD-platform based on the Finite Volume Method.The numerical results are validated with published experimental I–V curves for a hydrogen-fed anode-supported micro-tubular SOFC, and a numerical analysis of the influence of different operation conditions on the temperature distribution is performed to procure a better understanding of the heat management of the cell.

© 2011 Elsevier B.V. All rights reserved.

1. Introduction

The environmental concerns and the geopolitical consequences of the use of fossil fuels have prompted, in the last decades, the need for new and cleaner energy technologies. Hence, solid oxide fuel cells (SOFC) are increasingly regarded as a future environmental-friendly power-generation technology. Although some pre-commercial prototypes are already available [1,2], a wider use of SOFC still requires a research effort to reduce the high costs, to increase the durability and to improve their start-up performance. To reach these goals, current research is focused on the study of new cell materials and structures, which enable good cell performance at lower operating temperatures. The anode-supported microtubular SOFC is one of those promising new cell structures [3,5,6], since it offers high thermal shock resistance, rapid startability, lower operating temperatures, higher power densities and simpler seal requirements. However, mass transport and heat management become critical during the operation of such micro-tubular cells, since the high power density enhances Joule heating and the thick anode hinders the supply of the reactants to the reaction sites. Since the species and temperature distribu-

tions within the cell are not easy to measure, numerical simulations are being increasingly employed to understand the experimental evidence and to steer the cell optimization [4].

The modeling by the authors of mass-transfer in SOFCs was already addressed in a previous paper [7,8], where multimodal mass-transfer was thoroughly studied under isothermal conditions. In this paper, heat transfer issues in SOFCs are explored. It will be shown that the inlet temperatures of the gases play a critical role in the cell performance, in particular when the feeding velocities are large and the gases are not preheated. In these conditions, the convective cooling of the cell may lead to a degradation of performance that may be wrongly attributed.

To conduct the analysis, the pre-existing model is extended with heat-transfer capabilities. Hence, the model accounts not only for the mass and momentum conservation in the gas channels and electrodes and the electrochemistry; but also for the coupled heat transfer across the whole cell. Recent reviews on SOFC modeling [9,10], indicate that models with heat-transfer features have indeed been reported in the past; among these, the authors would like to highlight the comprehensive modeling presented by Serincan et al. [27]. The novelty introduced by the present work is multifacted. Mathematically, a new formulation to solve the coupled heat transfer within the cell is presented (see Section 2), where the sensible-enthalpy conservation-equation is derived in terms of temperature avoiding the use of constant thermodynamic properties. The temperature-dependence of the transport and ther-

* Corresponding author at: Área de Mecánica de Fluidos (CPS), C/María de Luna 3, 50018 Zaragoza, Spain. Tel.: +34 976762153; fax: +34 976761882.
E-mail address: Norberto.Fueyo@unizar.es (N. Fueyo).

Nomenclature

a	Constant, Eq. (37)
A	Area (m^2)
b	Constant, Eq. (37)
B_o	Permeability of the porous-medium (m^2)
C_p	Specific heat at constant pressure of the fluid ($m^2\,s^{-2}\,K^{-1}$)
$D_{\alpha\beta}$	Binary diffusion coefficient of species α in species β ($m^2\,s^{-1}$)
$D_{\alpha m}$	Diffusion coefficient of species α in the gas mixture ($m^2\,s^{-1}$)
$D_{\alpha\beta}^{eff}$	Effective binary diffusion coefficient of species α in species β ($m^2\,s^{-1}$)
$D_{\alpha K}^{eff}$	Effective Knudsen diffusion coefficient of species α ($m^2\,s^{-1}$)
E	Energy ($kg\,m^2\,s^{-2}\,kmol^{-1}$)
E^o	Standard electrochemical cell voltage (V)
E_b	Blackbody emissive power
f	Body forces ($m\,s^{-2}$)
F	Faraday's constant ($A\,s\,kmol^{-1}$)
F_{i-j}	View factor between surface i and surface j
h	Sensible enthalpy of the fluid ($m^2\,s^{-2}$)
h_α	Sensible enthalpy of the species α in the fluid ($m^2\,s^{-2}$)
H_o	Incident radiation entering or leaving the enclosure through an opening ($kg\,s^{-3}$)
$\vec{i}$	Unit vector in the direction of x-axis
I	Current density ($A\,m^{-2}$)
I_o	Exchange current density ($A\,m^{-2}$)
$\vec{j}_\alpha$	Mass diffusive flux of species α ($kg\,m^{-2}\,s^{-1}$)
k_B	Boltzmann's constant ($kg\,m^2\,s^{-2}\,K^{-1}$)
l	Thickness (m)
n	Number of electrons to convert a single molecule of species α
$\vec{n}$	Normal unit-vector
$\vec{N}_\alpha$	Total molar flux of species α ($kmol\,m^{-2}\,s^{-1}$)
p	Pressure ($kg\,m^{-1}\,s^{-2}$)
p_α	Partial pressure of species α ($kg\,m^{-1}\,s^{-2}$)
P	Power ($kg\,m^2\,s^{-3}$)
$\vec{q}$	Energy flux ($kg\,s^{-3}$)
Q	Volumetric heat sources, Joule heat ($kg\,m^{-1}\,s^{-3}$)
Q_{in}	Volumetric inlet flow ($m^3\,s^{-1}$)
$\vec{r}$	Vector from channel surface to enclosure (m)
R	Ideal gas constant ($kg\,m^2\,s^{-2}\,kmol^{-1}\,K^{-1}$)
S	Volumetric mass source ($kg\,m^{-3}\,s^{-1}$)
S_α	Volumetric mass source of species α ($kg\,m^{-3}\,s^{-1}$)
S_λ	Sutherland-law parameter (K)
S_μ	Sutherland-law parameter (K)
T	Temperature (K)
$T_{0\lambda}$	Sutherland-law parameter (K)
$T_{0\mu}$	Sutherland-law parameter (K)
$\vec{v}$	Fluid velocity ($m\,s^{-1}$)
V	Voltage (V)
W_α	Molecular weight of species α ($kg\,kmol^{-1}$)
x_α	Molar fraction of species α in the gas mixture
y_α	Mass fraction of the species α

Greek symbols

α	Gas mixture species
$\bar{\alpha}$	Backward transfer coefficient
$\vec{\alpha}$	Forward transfer coefficient
β	Gas mixture species
γ	Pre-exponential coefficient ($A\,m^{-2}$)
Γ_α^*	Dusty-gas model parameter ($kg^{-1}\,s\,kmol$)
ε	Porosity
ε_α	Characteristic Lennard-Jones energies of species α ($kg\,m^2\,s^{-2}$)
ε_{rad}	Emissivity of the surface
η	Overpotential (V)
θ	Angle
λ	Thermal conductivity of the fluid ($kg\,m\,s^{-3}\,K^{-1}$)
λ_s	Thermal conductivity of the solid ($kg\,m\,s^{-3}\,K^{-1}$)
λ^{eff}	Effective thermal conductivity of the fluid and porous medium as a continuum ($kg\,m\,s^{-3}\,K^{-1}$)
λ_o	Sutherland-law parameter ($kg\,m\,s^{-3}\,K^{-1}$)
μ	Viscosity of the fluid ($kg\,m^{-1}\,s^{-1}$)
μ_α	Viscosity of species α ($kg\,m^{-1}\,s^{-1}$)
μ_o	Sutherland-law parameter ($kg\,m^{-1}\,s^{-1}$)
ρ	Fluid density ($kg\,m^3$)
σ	Anionic conductivity ($A\,V^{-1}\,m^{-1}$)
$\sigma_{\alpha\beta}$	Collision diameter (Lennard-Jones 12-6 potential model) (Å)
σ_α	Characteristic length of species α (Å)
σ_{S-B}	Stefan-Boltzmann constant ($kg\,s^{-3}\,K^{-4}$)
τ	Tortuosity factor
$\vec{\bar{\tau}}'$	Viscous stress tensor ($kg\,m^{-1}\,s^{-2}$)
$\vec{v}_\alpha^{p*}$	Dusty-gas model parameter ($kg^{-1}\,s\,kmol$)
$\vec{v}_\alpha^{N*}$	Dusty-gas model parameter ($kg^{-1}\,s\,kmol$)
ϕ_v	Viscous dissipation ($kg\,m^{-1}\,s^{-3}$)
ϖ	Heat of reaction ($kg\,m^{-1}\,s^{-3}$)
ϖ'	Molar reaction heat release ($kg\,m^2\,s^{-2}\,kmol^{-1}$)
Ω_D	Collision integral

Subscripts

a	Anode
act	Activation
c	Cathode
CI	Channel interface coupled to the electrode
con	Concentration
e	Electrolyte
EI	Electrode interface coupled to the channel
fuel	Fuel
i	Index for channel isothermal differential surfaces
in	Channel inlet
j	Index for enclosure isothermal differential surfaces
new	New iteration
ocv	Open circuit voltage
ohm	Ohmic
out	Channel outlet
oven	Heated furnace wall
rad	Radiation
ref	Reference
rw	Reaction wall, active electrode–electrolyte interface

modynamic properties of the gases and solid components of the cell is fully considered, enhancing the accuracy of the temperature calculation. From the point of view of Computational Fluid Dynamics (CFD), unlike most of the previous SOFC models, which are based on ad-hoc extensions to commercial codes, the numerical algorithm presented in this paper (Section 3) has been fully implemented by the authors in OpenFOAM, an open-source CFD platform. Finally, in Section 4, the model has been exploited from a scientific point of view to get a better understanding of the heat management in SOFCs. In Section 4, the validity of the model is proved by comparison of its results against experimental data [5]; and it is then

used to study the cooling effect of the feeding fuel on the cell performance.

2. Mathematical model

In this section, the mathematical model that describes the steady-state operation of a solid oxide fuel cell is described. This model is based on a previous one by the same authors for mass-transfer in SOFCs [7,8], which has been extended to consider other relevant phenomena involved in the SOFC operation: heat transfer and electrochemistry. Due to multiphysics nature of SOFCs, the model consists of four subsets of equations: (i) channel model; (ii) electrode model; (iii) electrolyte model; and (iv) electrochemistry model.

2.1. Channel model

The set of equations solved to model both channels are continuity, momentum, species and enthalpy conservation-equations.

The continuity equation is:

$$\nabla \cdot (\rho \vec{v}) = S \tag{1}$$

where ρ is the fluid density, $\vec{v}$ is the fluid velocity in the channel and S is the volumetric mass source term. The momentum-conservation equations are:

$$\nabla \cdot (\rho \vec{v} \vec{v}) - \nabla \cdot \vec{\vec{\tau}}' = -\nabla p \tag{2}$$

where $\vec{\vec{\tau}}'$ is the viscous stress tensor and p is the pressure. The equation for the conservation of the chemical species α is written as:

$$\nabla \cdot (\rho y_\alpha \vec{v}) + \nabla \cdot \vec{j}_\alpha = S_\alpha \tag{3}$$

where y_α is the mass fraction of the species α, $\vec{j}_\alpha$ is the mass diffusive flux of species α, and S_α is the volumetric source term for the species α. The multicomponent diffusion is modelled using a consistent effective binary diffusion method [11]:

$$\vec{j}_\alpha = -\rho D_{\alpha m} \nabla y_\alpha + y_\alpha \rho \sum_{\forall \beta} D_{\beta m} \nabla y_\beta \tag{4}$$

where $D_{\alpha m}$ is the diffusion coefficient of species α in the gas mixture, given by:

$$D_{\alpha m} = \frac{1 - x_\alpha}{\sum_{\beta \neq \alpha} x_\beta / D_{\alpha \beta}} \tag{5}$$

Here, x_α is the molar fraction of species α and $D_{\alpha \beta}$ is the binary diffusion coefficient of species α in species β, modelled as [13]:

$$D_{\alpha \beta} = 2.628 \times 10^{-3} \frac{\sqrt{T^3 (W_\alpha + W_\beta / 2 W_\alpha W_\beta)}}{\sigma_{\alpha \beta}^2 \Omega_D p} \tag{6}$$

where W_α and W_β are the molecular weights of species α and β respectively; $\sigma_{\alpha \beta}$ is the collision diameter (Lennard-Jones 12-6 potential model) given by $\sigma_{\alpha \beta} = (\sigma_\alpha + \sigma_\beta)/2$, with σ_α and σ_β being the characteristic length of species α and β; and Ω_D is the collision integral:

$$\Omega_D = \frac{1.06036}{(T^*)^{0.15610}} + \frac{0.1930}{\exp(0.47635 T^*)} + \frac{1.03587}{\exp(1.52996 T^*)}$$
$$+ \frac{1.76474}{\exp(3.89411 T^*)} \tag{7}$$

Here, $T^* = k_B T (\varepsilon_\alpha \varepsilon_\beta)^{-0.5}$, where k_B is the Boltzmann's constant and ε_α and ε_β are the characteristic Lennard-Jones energies of species α and β respectively [14]. Data for ε_α, ε_β, σ_α and σ_β are taken from [15].

Finally, energy conservation in the system is considered through the sensible-enthalpy equation:

$$\nabla \cdot (\rho h \vec{v}) + \nabla \cdot (\vec{q}) = \vec{v} \cdot \nabla p + \phi_v + Q + \rho \sum_\alpha y_\alpha f_\alpha \vec{v}_\alpha + \varpi \tag{8}$$

where h is the sensible enthalpy of the fluid ($h = \sum_\alpha y_\alpha h_\alpha$), $\vec{q}$ is the energy flux, ϕ_v is the viscous dissipation, Q represents the volumetric heat sources, f_α accounts for the body forces and ϖ for the heat of reaction. The following assumptions apply to the study of the SOFC operation: the effect of body forces has no relevance on the system energy ($\rho \sum_\alpha y_\alpha f_\alpha \vec{v}_\alpha \approx 0$); energy dissipation due to viscous forces in gas flows under laminar regime may be neglected ($\phi_v \approx 0$); energy sources due to compressibility effects are ignored, since large pressure differences are not expected inside the cell ($\vec{v} \cdot \nabla p \approx 0$); and the heat flux accounts for the heat conduction and the heat flux due to species diffusion with different enthalpies ($\vec{q} = -\lambda \nabla T + \sum_\alpha \vec{j}_\alpha h_\alpha$). Then, Eq. (8) is simplified to:

$$\nabla \cdot (\rho h \vec{v}) - \nabla \cdot (\lambda \nabla T) + \nabla \cdot \left(\sum_\alpha (\vec{j}_\alpha h_\alpha) \right) = Q + \varpi \tag{9}$$

In the SOFC channels, the reaction heat release is zero ($\varpi = 0$), because the reaction sites are located in the electrodes. According to previous studies [20,21], the gases in the SOFC can be regarded as non-participating media for radiation. In the cathodic channel, the air consists of simple non-polar molecules, transparent to radiation. In the anodic channel, the radiation of the participating species has been shown to have a negligible effect on the SOFC performance, under normal SOFC operation conditions. Thus a surface-to-surface radiation model has been used and will be described later; but, for the fluids in the channels, there are no volumetric heat sources due to radiation and $Q = 0$ above. The final-heat transfer equation is therefore:

$$\nabla \cdot (\rho h \vec{v}) - \nabla \cdot (\lambda \nabla T) + \nabla \cdot \left(\sum_\alpha (\vec{j}_\alpha h_\alpha) \right) = 0 \tag{10}$$

Considering the definition of the sensible enthalpy ($dh = C_p dT$), Eq. (10) may be rewritten as:

$$\nabla \cdot (\rho C_p \vec{v} T) - \nabla \cdot (\lambda \nabla T) = T \nabla \cdot (C_p \rho \vec{v}) - \nabla \cdot \left(\sum_\alpha (\vec{j}_\alpha h_\alpha) \right) \tag{11}$$

where C_p is the fluid specific heat at constant pressure ($C_p = \sum_\alpha y_\alpha C_{p\alpha}$), λ is the thermal conductivity of the fluid and h_α is the sensible enthalpy of the species α in the fluid. These properties of the fluid are temperature dependent. The JANAF thermochemical tables are used to calculate the specific heat at constant pressure and the sensible enthalpy for each species α in the fluid:

$$C_{p\alpha} = \frac{R}{W_\alpha} (a_{1\alpha} + a_{2\alpha} T + a_{3\alpha} T^2 + a_{4\alpha} T^3 + a_{5\alpha} T^4) \tag{12}$$

$$h_\alpha = \int_{T_{ref}=0}^{T} C_{p\alpha} dT$$
$$= \frac{R}{W_\alpha} \left(a_{1\alpha} T + \frac{a_{2\alpha}}{2} T^2 + \frac{a_{3\alpha}}{3} T^3 + \frac{a_{4\alpha}}{4} T^4 + \frac{a_{5\alpha}}{5} T^5 \right) \tag{13}$$

where $a_{1\alpha}$, $a_{2\alpha}$, $a_{3\alpha}$, $a_{4\alpha}$, $a_{5\alpha}$ are the JANAF constants [17]. The semi-empirical formula of Wilke (1950) is used to estimate the multicomponent-fluid thermal-conductivity [16]:

$$\lambda = \sum_{\forall \alpha} \frac{x_\alpha \lambda_\alpha}{\sum_{\forall \beta} x_\beta \phi_{\alpha \beta}} \tag{14}$$

where

$$\phi_{\alpha \beta} = \frac{\left[1 + (\lambda_\alpha / \lambda_\beta)^{1/2} (W_\beta / W_\alpha)^{1/4} \right]^2}{(8 + 8 \ W_\alpha / W_\beta)^{1/2}} \tag{15}$$

The Sutherland model accounts for the temperature dependence of the thermal conductivity of each species α in the fluid:

$$\lambda_\alpha = \lambda_{o\alpha} \left(\frac{T}{T_{o\lambda\alpha}}\right)^{3/2} \frac{T_{o\lambda\alpha} + S_{\lambda\alpha}}{T + S_{\lambda\alpha}} \tag{16}$$

where the Sutherland-law parameters (λ_o, $T_{0\lambda}$, S_λ) are tabulated for the most common gases in [16].

2.2. Electrode model

In the electrodes, the same physical phenomena as in the channels are studied. However, the governing equation for each phenomenon differs from that in the channel due to the porous nature of the electrodes. The momentum conservation-equation is formulated in the form of Darcy's Law:

$$\vec{v} = -\frac{B_o}{\mu} \nabla p \tag{17}$$

where $\vec{v}$ represents the superficial permeation velocity, B_o the porous-medium permeability, p the pressure, and μ the gas-mixture viscosity. Eq. (14) is similarly applied to estimate the viscosity of the multicomponent fluid:

$$\mu = \sum_{\forall \alpha} \frac{x_\alpha \mu_\alpha}{\sum_{\forall \beta} x_\beta \phi_{\alpha\beta}} \tag{18}$$

where μ_α represents the viscosity of each of the species α in the gas mixture and $\phi_{\alpha\beta}$ is given by:

$$\phi_{\alpha\beta} = \frac{\left[1 + (\mu_\alpha/\mu_\beta)^{1/2}(W_\beta/W_\alpha)^{1/4}\right]^2}{(8 + 8\ W_\alpha/W_\beta)^{1/2}} \tag{19}$$

The viscosity of each species α is estimated from the Sutherland law, as follows:

$$\mu_\alpha = \mu_{o\alpha} \left(\frac{T}{T_{o\mu\alpha}}\right)^{3/2} \frac{T_{o\mu\alpha} + S_{\mu\alpha}}{T + S_{\mu\alpha}} \tag{20}$$

The Sutherland-law parameters μ_o, $T_{0\mu}$, S_μ are tabulated in [16]. Pressure is calculated from the mixture composition using the equation:

$$p = \sum_{\forall \alpha} p_\alpha \tag{21}$$

where p_α is the partial pressure of species α.

The equation for the conservation of the chemical species α in the gas mixture is:

$$\nabla \cdot \vec{N}_\alpha = 0 \tag{22}$$

where $\vec{N}_\alpha$ is the total molar flux of species α, given by the Dusty Gas Model [12]:

$$-\frac{\nabla p_\alpha}{RT} = \frac{1}{p} \sum_{\beta \neq \alpha} \frac{p_\beta \vec{N}_\alpha - p_\alpha \vec{N}_\beta}{D_{\alpha\beta}^{\text{eff}}} + \frac{\vec{N}_\alpha}{D_{\alpha K}^{\text{eff}}} + \frac{p_\alpha}{RT} \frac{B_o}{D_{\alpha K}^{\text{eff}} \mu} \nabla p \tag{23}$$

where R is the ideal gas constant, T is the fluid temperature, $D_{\alpha\beta}^{\text{eff}}$ is the effective binary diffusion coefficient of species α in species β:

$$D_{\alpha\beta}^{\text{eff}} = \frac{\varepsilon}{\tau} D_{\alpha\beta} \tag{24}$$

where ε is the electrode porosity, τ is the electrode tortuosity factor and $D_{\alpha\beta}$ is given by Eq. (6); and $D_{\alpha K}^{\text{eff}}$ is the effective Knudsen diffusion coefficient of species α [18]:

$$D_{\alpha K}^{\text{eff}} = \frac{\varepsilon}{\tau} \frac{d_p}{3} \sqrt{\frac{8RT}{\pi W_\alpha}} \tag{25}$$

After some manipulation of Eq. (23), $\vec{N}_\alpha$ may be expressed as:

$$\vec{N}_\alpha = -\Gamma_\alpha^* \nabla p_\alpha + \vec{v}_\alpha^{p*} p_\alpha + \vec{v}_\alpha^{N*} p_\alpha \tag{26}$$

where:

$$\Gamma_\alpha^* = \frac{1}{RT \left(\sum_{\beta \neq \alpha} x_\beta/D_{\alpha\beta}^{\text{eff}} + 1/D_{\alpha K}^{\text{eff}}\right)} \tag{27}$$

$$\vec{v}_\alpha^{p*} = \Gamma_\alpha^* \left(-\frac{B_o}{D_{\alpha K}^{\text{eff}} \mu} \nabla p\right) = \frac{\Gamma_\alpha^*}{D_{\alpha K}^{\text{eff}}} \vec{v} \tag{28}$$

$$\vec{v}_\alpha^{N*} = \Gamma_\alpha^* \frac{RT}{p} \sum_{\beta \neq \alpha} \frac{\vec{N}_\beta}{D_{\alpha\beta}^{\text{eff}}} \tag{29}$$

Further details of the above manipulation, for the isothermal case, are given in [7]. The physical meaning and relative relevance of Γ_α^*, $\vec{v}_\alpha^{p*}$ and $\vec{v}_\alpha^{N*}$ are investigated in [8], also for the isothermal case. Inserting Eq. (26) into Eq. (22), the conservation-equation for the species α may be expressed as follows:

$$-\nabla \cdot (\Gamma_\alpha^* \nabla p_\alpha) + \nabla \cdot (\vec{v}_\alpha^{p*} p_\alpha) + \nabla \cdot (\vec{v}_\alpha^{N*} p_\alpha) = 0 \tag{30}$$

Reaction source terms are not present on the right hand side of Eq. (30) because the electrochemical reaction is modelled as a superficial reaction. The species sources or sinks in the electrodes are given by Faraday's law and are treated as boundary conditions at the electrode–electrolyte interface (reaction wall, *rw*):

$$\vec{N}_{\alpha,rw} = \frac{I}{nF} \vec{n}_{rw} \tag{31}$$

where I is the current density at the reaction wall (I_a or I_c depending on the electrode; see Section 2.3), n represents the number of electrons to convert a single molecule of species α, F is the Faraday's constant and $\vec{n}_{rw}$ is the reaction-wall-normal unit vector. Finally, principle of energy conservation is applied to calculate the temperature profile within the electrodes. The following assumptions apply to the SOFC electrodes: (i) local-thermal equilibrium may be assumed between the porous matrix and the fluid flowing through the void space of the electrode, as reported in [23]; (ii) the volumetric heat sources within the electrodes are neglected since they are opaque bodies [20,24], and Joule heating is only considered within the electrolyte; (iii) $dh = C_p dT$; and (iv):

$$\nabla \cdot (\rho h \vec{v}) + \nabla \cdot \left(\sum_\alpha (\vec{j}_\alpha h_\alpha)\right) = \nabla \cdot \left(\sum_\alpha [W_\alpha \vec{N}_\alpha h_\alpha]\right) \tag{32}$$

From Eq. (9), the sensible enthalpy conservation equation in the electrodes turns into:

$$\nabla \cdot \left[\sum_\alpha (W_\alpha \vec{N}_\alpha C_{p\alpha})T\right] - \nabla \cdot (\lambda^{\text{eff}} \nabla T)$$

$$= \varpi + T\nabla \cdot \left[\sum_\alpha (W_\alpha \vec{N}_\alpha C_{p\alpha})\right] - \sum_\alpha [h_\alpha \nabla \cdot (W_\alpha \vec{N}_\alpha)] \tag{33}$$

where $C_{p\alpha}$, h_α, $\vec{N}_\alpha$ are given by Eqs. (12), (13) and (26) respectively; and λ^{eff} is the effective thermal conductivity of the fluid and porous medium as a continuum, modelled according to the upper Wiener bound [19]:

$$\lambda^{\text{eff}} = (1 - \varepsilon)\lambda_s + \varepsilon\lambda \tag{34}$$

where λ represents the thermal conductivity of the fluid and is given by Eq. (14), while λ_s is the thermal conductivity of the solid. The heat release due to the electrochemical reaction is assumed to take place on the anode side. Thus in Eq. (33): $\varpi = 0$ in the cathode; while in the anode the molar reaction-heat release is $\varpi' = -242000 - 6.05(T_{\text{ref}} - 298)$ [J mol^{-1}].

The effect of surface-to-surface radiative heat-exchange is included using a view-factor-based radiation-model. The model calculates, in the manner described in the Appendix, the heat flux $\vec{q}_{rad}$ arriving at or departing the surfaces of the electrodes from or to all of the surfaces in the domain; this flux is included in the energy equation for the electrodes as a boundary condition.

2.3. Electrolyte model

The electrolyte is an impervious solid, that impedes gas flow. Nevertheless, there are mass and charge transport, and heat release, due to the anionic (O^{2-}) current. The charge transport is assumed to be one-directional (normal to the reaction walls); this assumption is valid for thin electrolytes, such those in the microtubular anode-supported cells ($\approx 20\,\mu m$). In tubular cells the reaction area in the cathode (A_c) differs from that in the anode (A_a) since the electrolyte has a finite thickness. Hence, the current densities at both reaction walls (active electrode–electrolyte interfaces) satisfy the following relationship, which ensures charge and mass conservation in the electrolyte:

$$I_a = \frac{A_c}{A_a} I_c \tag{35}$$

Heat transfer through the impervious electrolyte is only possible by means of conduction and radiation mechanisms. The effect of radiation within the state-of-the-art very thin electrolytes has been found to be negligible [20,24]. Conduction is thus the only relevant heat-transfer mechanism. Thus, from Eq. (9):

$$-\nabla \cdot (\lambda \nabla T) = Q + \varpi \tag{36}$$

where $\varpi = 0$ because the reaction heat is considered to be entirely released in the anode; and the volumetric heat sources are, in absence of radiation, only due to the ohmic heating ($Q = Q_{ohm}$), also known as Joule heating:

$$-\nabla \cdot (\lambda \nabla T) = Q_{ohm} \tag{37}$$

where:

$$Q_{ohm} = \frac{I_e^2}{\sigma_e} \tag{38}$$

where the mean current density in the electrolyte is estimated as $I_e = (I_a + I_c)/2$; and the electrolyte anionic conductivity, σ_e, is given by:

$$\sigma_e = a_e \exp\left(\frac{-b_e}{T}\right) \tag{39}$$

a_e and b_e are constants tabulated in [25] for the common electrolyte materials.

The effect of surface-to-surface radiative heat-exchange is included, as for the electrodes, as a boundary condition (see Appendix).

2.4. Electrochemical model

The electrochemical reaction that takes place in a H_2-fed SOFC consists in the oxidation of the hydrogen in the anode and the reduction of oxygen in the cathode, releasing a water molecule as a product in the anode:

$$H_2 \rightarrow 2H^+ + 2e^- \,(\text{anode}) \tag{40}$$

$$1/2O_2 + 2e^- \rightarrow O^{2-} \,(\text{cathode}) \tag{41}$$

$$2H^+ + O^{2-} \rightarrow H_2O \,(\text{anode}) \tag{42}$$

The overall electrochemical reaction is described as follows:

$$H_2 + 1/2O_2 \rightarrow H_2O \tag{43}$$

The total electromotive force of the above electrochemical system is described by the Nernst equation. However, during operation, the real voltage of a cell is smaller than that predicted by Nernst due to the cell resistances, and then the voltage of the cell is given by

$$V = \underbrace{E^o + \frac{RT}{2F}\ln\left(\frac{p_{H_2}\sqrt{(p_{O_2}/p_{ref})}}{p_{H_2O}}\right) - \eta_{ohm} - (\eta_{act} + \eta_{con})_a}_{V_{ocv}}$$
$$- (\eta_{act} + \eta_{con})_c \tag{44}$$

where E^o is the standard electrochemical cell voltage, $E^o = 1.271 - 2.731 \times 10^{-4}T$; the partial pressures of the involved species are referred to the feeding streams compositions; and η_{con}, η_{ohm}, η_{act} stand for the concentration, ohmic and activation losses. The concentration polarization is due to mass transport resistances in the electrodes; it is calculated as follows:

$$\eta_{con,a} = \frac{RT}{2F}\ln\left(\frac{p_{H_2}p_{H_2O,rw}}{p_{H_2O}p_{H_2,rw}}\right) \tag{45}$$

$$\eta_{con,c} = \frac{RT}{2F}\ln\left(\frac{\sqrt{p_{O_2}}}{\sqrt{p_{O_2,rw}}}\right) \tag{46}$$

where $p_{\alpha,rw}$ is the partial pressure of the species α at the electrode–electrolyte interface (reaction wall). The ohmic polarization is mainly caused by the resistance to the transport of oxygen-anions through the electrolyte; it may be estimated as:

$$\eta_{ohm} = \frac{\delta l_e}{\sigma_e} I_e \tag{47}$$

where l_e is the electrolyte thickness. Finally, the Butler-Volmer equation provides the relationship between the current density and the activation polarization of the electrode. The most general form of the Butler-Volmer equation is:

$$I = I_o\left[\exp\left(\frac{\bar{\alpha}F\eta_{act}}{RT}\right) - \exp\left(\frac{-\bar{\alpha}F\eta_{act}}{RT}\right)\right] \tag{48}$$

where $\bar{\alpha}$ and $\tilde{\alpha}$ are the backward and forward transfer coefficients and I_o is the exchange current density, the calculation of which for both electrodes uses the following experimental correlations [26]:

$$I_{o,a} = \gamma_a\left(\frac{p_{H_2}}{p_{ref}}\right)\left(\frac{p_{H_2O}}{p_{ref}}\right)^{-0.5}\exp\left(-\frac{E_{act,a}}{RT}\right) \tag{49}$$

$$I_{o,c} = \gamma_c\left(\frac{p_{O_2}}{p_{ref}}\right)^{0.25}\exp\left(-\frac{E_{act,c}}{RT}\right) \tag{50}$$

where γ_a and γ_c are the anodic and cathodic pre-exponential coefficients and $E_{act,a}$ and $E_{act,c}$ are the anodic and cathodic activation energies. Eq. (49) applied to both electrodes provides the corresponding activation overpotentials: $\eta_{act,a}$ and $\eta_{act,c}$.

3. Numerical details

The domain considered for the simulation of an anode-supported micro-tubular SOFC consists of five concentric and adjacent cylindrical sub-domains, viz. from the axis outwardly: (i) the fuel channel; (ii) the anode; (iii) the electrolyte; (iv) the cathode; and (v) the air channel. The axial symmetry of the tubular geometry simplifies the three-dimensional problem to a two-dimensional one. Thus, each of the submodels described in Section 2 is solved in its corresponding two-dimensional mesh and the respective solutions are coupled as required through boundary conditions. Fig. 1a shows a schematic of the domain, representing an anode-supported micro-tubular cell inside a cylindrical furnace.
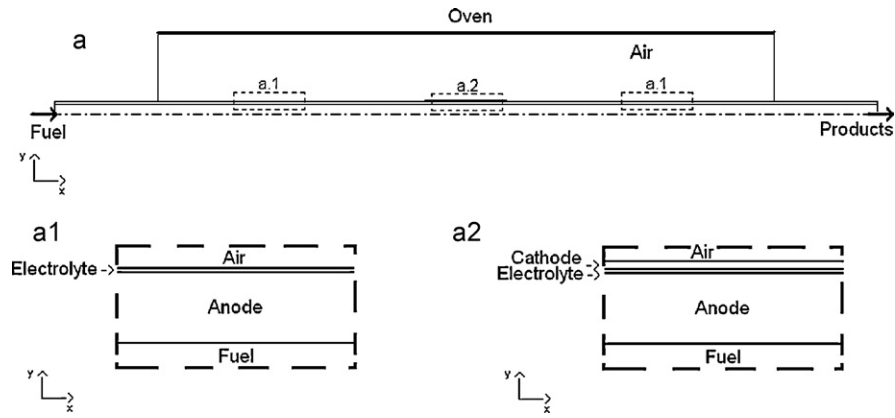
Fig. 1. Domain diagram.

The anode and the electrolyte are longer than the oven to allow the use of low-temperature seals; the cathode, i.e. the cell active area, is centered in the furnace (Fig. 1a.1) for the cell to operate at conditions as close as possible to isothermal ones.

The channel, electrode and electrolyte models, described in Section 2, are solved numerically using the finite-volume method. Fig. 2 is a schematic representation of the solution algorithm (black-solid lines) and the coupling paths between fields of adjacent meshes (dashed lines); the sub-indexes stand for the channel inlet (in), the channel outlet (out), the heated furnace wall (oven), the electrode–electrolyte reaction walls (rw), the channel interface coupled to the electrode (CI), and the electrode interface coupled to the channel (EI). In the channels, the continuity and momentum equations are solved using SIMPLE [27]. In the continuity equation (Eq. (1)), the volumetric mass source term (S) is zero throughout the domain. However, in the channel-electrode coupled boundary, a correction is applied to ensure continuity through both domains. In the electrode domain, continuity is fulfilled by the total molar fluxes given by the DGM ($\vec{N}_\alpha$) but not by the velocity given by Darcy's

law; continuity through the coupled boundary is thus achieved as follows: (i) $\vec{v}_{CI} = \vec{v}_{EI}$ and (ii) $S_{CI} = \sum_\alpha (\vec{N}_{\alpha,EI} W_\alpha) - \vec{v}_{CI} \rho_{CI}$. Similarly, in Eq. (3) $S_{\alpha,CI} = \vec{N}_{\alpha,EI} W_\alpha - \vec{v}_{CI} \rho_{CI} y_{\alpha,CI}$. The noteworthy feature of this algorithm is the absence of coupling between the temperature fields, due to the use of a coupled-matrix algorithm to solve simultaneously Eqs. (11), (33) and (37). Further details of the mass-, momentum- and species-fields coupling are given in [7].

The electrochemical algorithm is solved iteratively and this is also shown in Fig. 2 (dotted lines). The cell voltage, V, is the model input and is assumed constant through the cell active area. The mathematical model is initially solved with a guessed current density field at the cathode reaction wall; the current density for the next iteration step, $I_{c,new}$, is then calculated as follows:

$$I_{c,new} = \frac{V_{ocv} - V}{\eta_{ohm} + (\eta_{act} + \eta_{con})_a + (\eta_{act} + \eta_{con})_c} I_c \quad (51)$$

$I_{a,new}$ is then calculated from Eq. (34). The new estimated current density is not necessarily constant along the electrodes since the
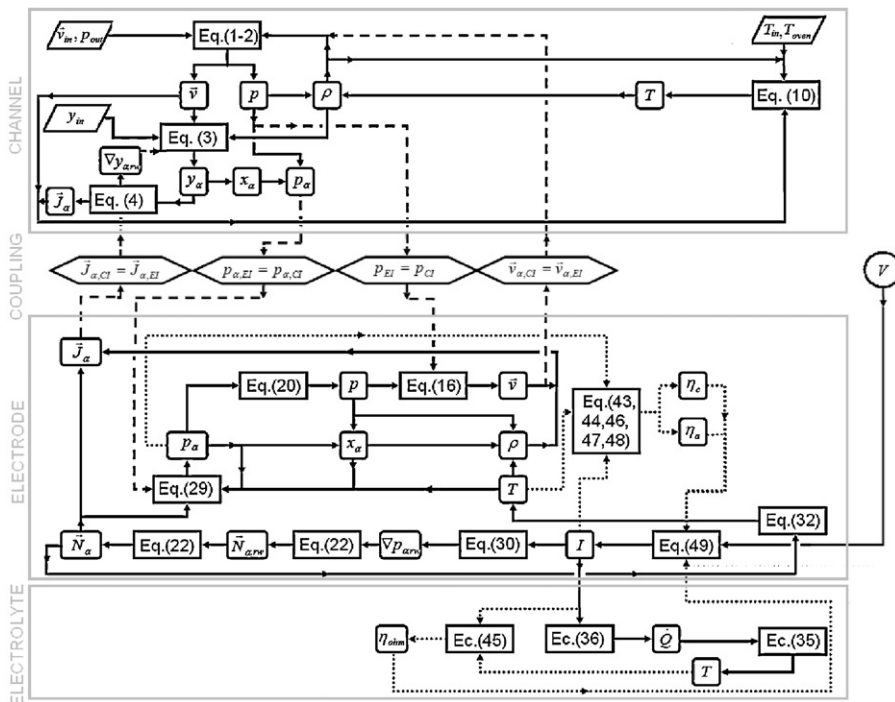

Fig. 2. Numerical algorithm. Coupling paths are shown in dashed lines and the electrochemical loop in dotted lines.

Table 1
Cell geometry and operating conditions.

Cell geometry [5]	
Fuel channel internal radius	1.2 mm
Anode thickness	400 μm
Electrolyte thickness	20 μm
Cathode thickness	50 μm
Air channel external radius[a]	1 cm
Fuel channel length	10 cm
Anode length	10 cm
Electrolyte length	10 cm
Cathode length	1 cm
Air channel length[a]	7.5 cm
Microstructural parameters [28]	
Anode porosity	41.4%
Anode tortuosity factor	3
Anode mean pore diameter	1.2 μm
Anode permeability	7.65e-15 m^2
Cathode porosity[b]	50%
Cathode tortuosity factor[b]	3
Cathode mean pore diameter[b]	1 μm
Cathode permeability[b]	7.65e-15 m^2
Operating conditions [5]	
Oven set temperature, T_{oven}	1123 K
Fuel temperature at inlet, $T_{in,fuel}$	293 K
Operating pressure, p_{out}	100000 Pa
Fuel composition, $x_{\alpha,in} \rightarrow H_2:H_2O:Ar$	4.85: 3: 92.15%
Air composition, $x_{\alpha,in} \rightarrow O_2:N_2$	21: 79%
Fuel inlet (@room), forced convection, $Q_{in,fuel}$	0.21 min^{-1}
Air inlet, natural convection, $\vec{v}_{in}$	$0.01\vec{i}$ ms^{-1}

[a] Personal Communication.
[b] Unmeasured, typical value assumed.

cell overpotentials depend on the species and temperature distributions.

4. Results and discussion

4.1. Model validation

The performance of the mathematical model and the numerical algorithm presented in Sections 2 and 3 has been evaluated by simulating the behaviour of a real hydrogen-fed anode-supported micro-tubular SOFC and comparing the numerical results with the corresponding experimental data. The experimental I–V, I–P curves reported by Campana et al. (sample 2) in [5] are the selected data to carry out the validation. The cell geometry, the operating conditions and the electrochemical model parameters are summarized in Tables 1 and 2. In the absence of the experimental-characterization, typical values for the cathode microstructure have been assumed.

Table 2
Electrochemical and thermophysical properties.

| Electrochemical parameters	
$\tilde{\alpha}_a, \tilde{\alpha}_a, \tilde{\alpha}_c, \tilde{\alpha}_c$ [a]	0.5
$E_{act,a}, E_{act,c}$ [26]	120 kJ mol^{-1}
γ_a [b]	1e + 11 Am^{-2}
γ_c [b]	1e + 9 Am^{-2}
Thermal properties [25]	
Anode thermal conductivity	3 Wm^{-1} K^{-1}
Electrolyte thermal conductivity	2 Wm^{-1} K^{-1}
Cathode thermal conductivity	4 Wm^{-1} K^{-1}
Electrolyte emissivity	0.4
Cathode emissivity	0.4
Furnace emissivity	0.8
Electrical properties [25]	
a_e	85,000 Sm^{-1}
b_e	11,000 K

[a] Unmeasured, typical value assumed.
[b] Fitting parameters.
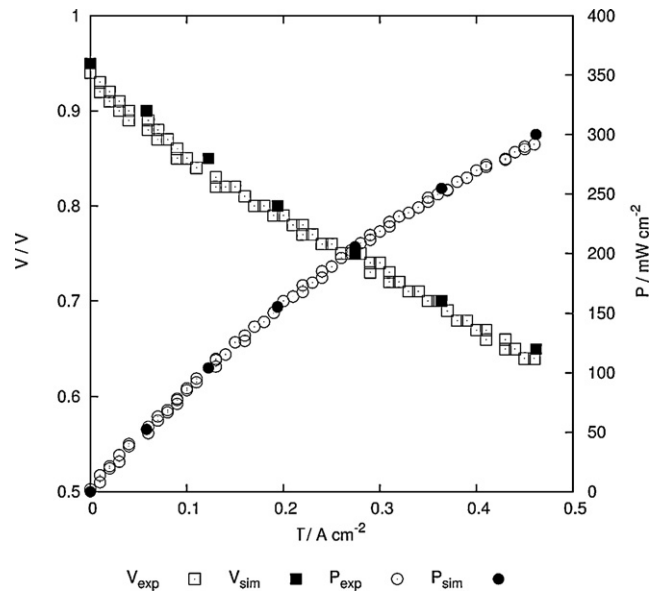
Fig. 3. Experimental data (open symbols) [5] vs simulation results (solid symbols) for the cell in Tables 1 and 2. The left axis is the cell voltage (V) and the right axis is the cell power ($P = IV$).

This assumption will not bear a significant influence on the results since the concentration overpotential in such thin cathode is negligible [5]. Numerical results are plotted in Fig. 3; where the x-axis represents the mean current density over the cathode-active area ($\bar{I} = A_c^{-1} \int_{A_c} I_c dA_c$); good agreement with the experimental curves is shown.

The contribution of each overpotential (mean value, $\bar{\eta}_* = A_*^{-1} \int_{A_*} \eta_* dA_*$) to the total voltage loss of the cell given in Table 1 is shown in Fig. 4. Again, the numerical results are in agreement with the experimental ones reported in [5]; the cathode-activation resistance and the anode-concentration resistance are the two main causes for the voltage-drop, while the cathode-concentration resistance may be neglected.

4.2. Discussion

As indicated in the Introduction, SOFC technology must still overcome some issues before becoming widely adopted commer-
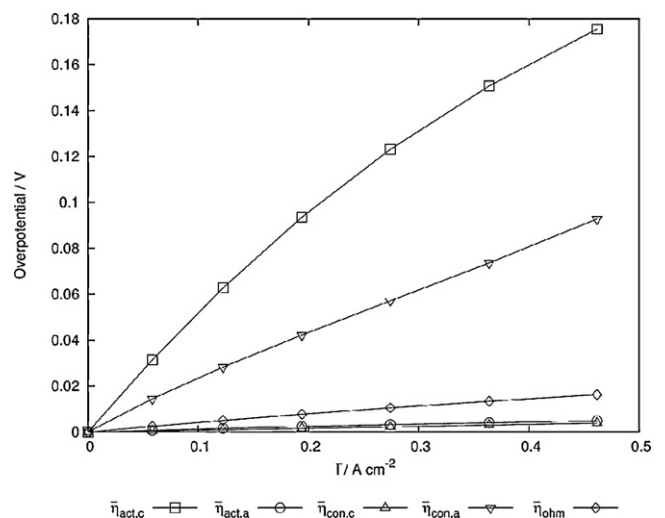

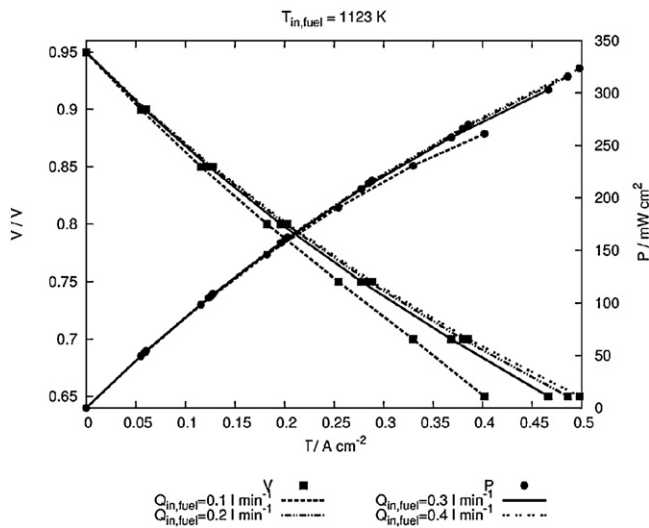**Fig. 4.** Mean overpotentials at different mean-current densities for the cell given in Tables 1 and 2.

Fig. 5. *I–V–P* curves for the cell given in Tables 1 and 2 with preheated fuel at different fuel flow-rates.
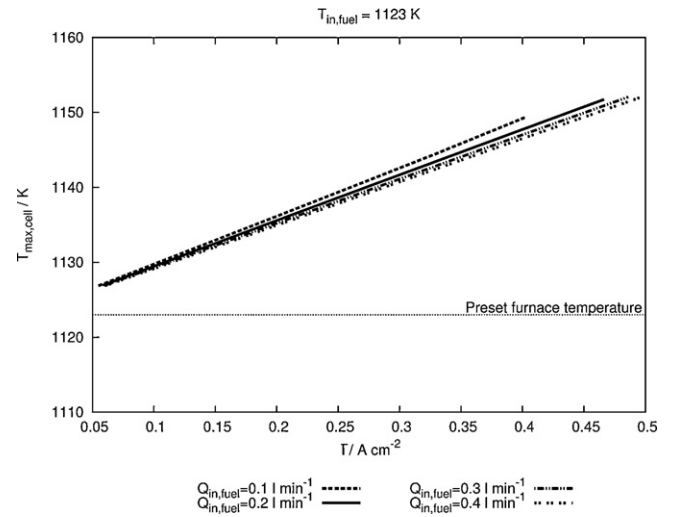

Fig. 7. Maximum cell temperature at different mean-current densities for the cell running with preheated fuel at different fuel flow-rates.

cially. Decreasing the operating temperature has been reported as one of the key factors to face those issues, since lower operating temperature brings about: (i) more economical cell sealants, thus reducing the overall SOFC costs; (ii) smaller cell thermal stresses, thus improving the cell reliability; (iii) faster start-ups; and (iv) smaller diffusion rates of the electrodes transition metals into the electrolyte, which reduces the degradation rate of the cell materials and improves their durability. Heat management thus plays an important role to minimize the temperature gradients and the hot spots within the SOFC. The temperature distribution is not easy to determine experimentally. Therefore, a numerical tool becomes essential to optimize the heat management of the SOFCs. Several numerical works on the temperature distribution in SOFCs may accordingly be found in the literature. For instance, Oulmi et al. [30] present a numerical study of the temperature distribution in a planar SOFC as a function of the SOFC configuration (anode or electrolyte supported); the model by Jeon et al. [31] is applied to

study the temperature field in a SOFC and its components along and across the cell at different loads; Qu et al. [32] predict the temperature distribution within an anode-supported planar SOFC with corrugated bipolar plates; and Serincan et al. [29] use their SOFC model to study the influence of the preset operating temperature on the cell performance and the temperature distribution. In all these numerical works, the authors have assumed the inlet temperature of the feeding gases (air & fuel) to be equal to the preset furnace-temperature. This assumption is often needed either because the experimental test rig is not described in detail, or to reduce the calculation time. However, the above assumption is only applicable if the gases are sufficiently preheated before reaching the cell active area; otherwise the gases may indeed cool down the cell, resulting in counter-intuitive cell performance, as it is illustrated below.

Suzuki et al. [4] reported a significant improvement in the performance of their anode-supported microtubular SOFC as they increased the fuel flow. This effect was numerically studied by Serincan et al. [29], who attributed the performance enhancement to
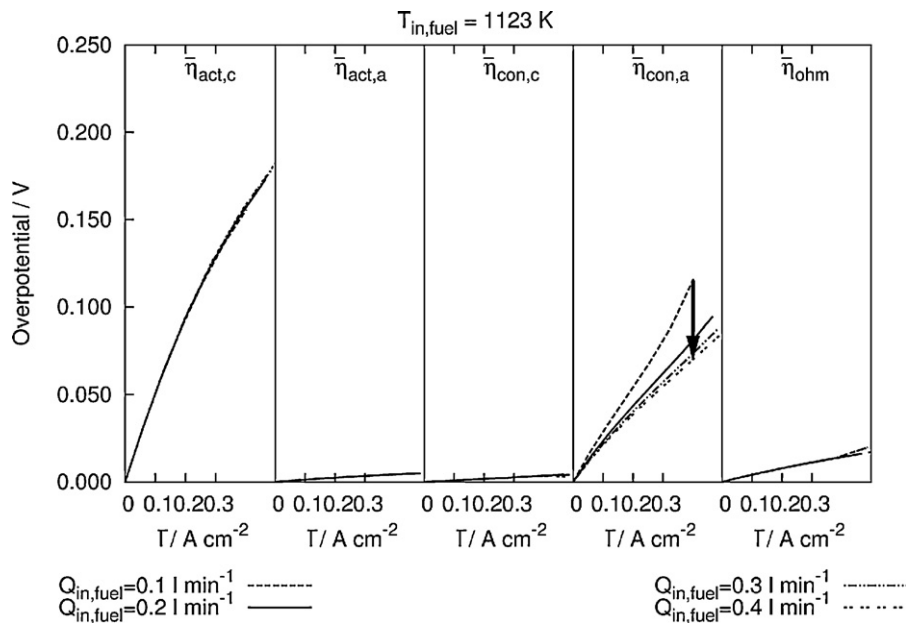

Fig. 6. Mean overpotentials at different mean current densities for the cell given in Tables 1 and 2 with preheated fuel at different fuel flow-rates.
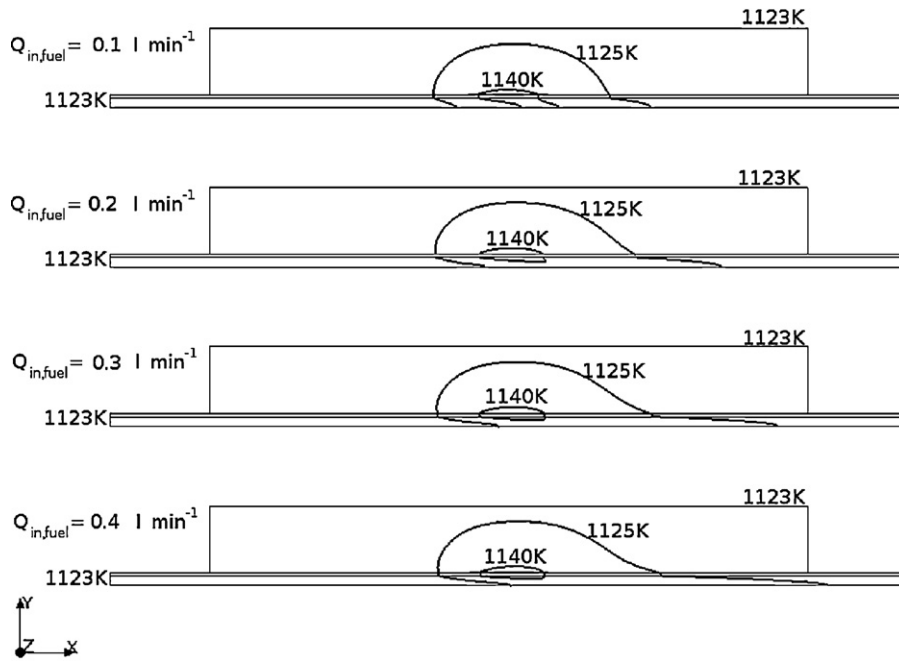
Fig. 8. Temperature contours (in Kelvin) for the cell given in Tables 1 and 2 with fuel preheating ($T_{in,fuel}$ = 1123 K) at 0.7 V and different fuel flow-rates. The cell active area is indicated with black straight line.

the decrease of the anode concentration-overpotential, remarking that the high fuel flow-rates increase the power output. In this section, the effect on this outcome of the widely used assumption that the fuel inlet temperature equals the oven temperature, $T_{in,fuel} = T_{oven}$, is studied for the cell given in Table 1, for which the fuel is usually fed at room temperature to the rig described in Fig. 1. The cell is thus simulated operating at four fuel flow-rates ($Q_{in,fuel}$ = 0.1, 0.2, 0.3, 0.4 l min^{-1}, referred to room temperature and pressure) and at two fuel inlet-temperatures, viz preheated flow ($T_{in,fuel} = T_{oven}$ = 1123 K) and room temperature ($T_{in,fuel}$ = 293 K, T_{oven} = 1123 K).

Fig. 5 shows the *I–V–P* for the given fuel inlet-flows assuming preheated fuel. The results show that high fuel flows improve the cell performance, which is in agreement with the experimental and numerical results of Suzuki et al. [4] and Serincan et al. [29]. The

results plotted in Fig. 6 also agree with Serincan's findings [29], i.e. the improvement of the cell performance when increasing the fuel flow is mainly due to a decrease in the anode concentration overpotential. The fuel flow-rate when the fuel is preheated does not alter significantly to the maximum temperature in the cell, as shown in Fig. 7, or the temperature distribution, as shown in Fig. 8, and so the temperature dependent overpotentials (η_{act}, η_{ohm}) remain almost constant, as shown in Fig. 6. However, Fig. 9 shows the *I–V–P* curves for the cell reported in [5] at different fuel flow-rates. The fuel is fed at room temperature as it is done in [5]. From Fig. 9 it is clear that the cell-performance improves as the fuel flow-rate is increased from 0.1 l min^{-1} to 0.2 l min^{-1}. However, if the fuel flow-rate is further increased the performance of the cell either does not improve (from 0.2 l min^{-1} to 0.3 l min^{-1}) or it even deteriorates (from 0.3 l min^{-1} to 0.4 l min^{-1}). As it is shown in Fig. 10, large fuel flow-rates decrease
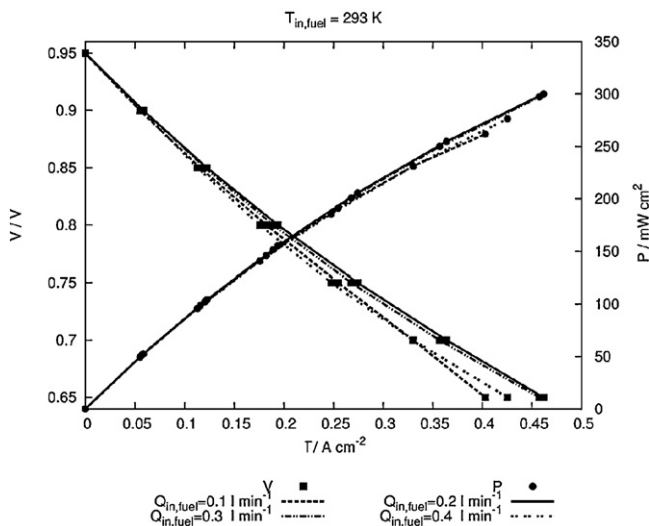

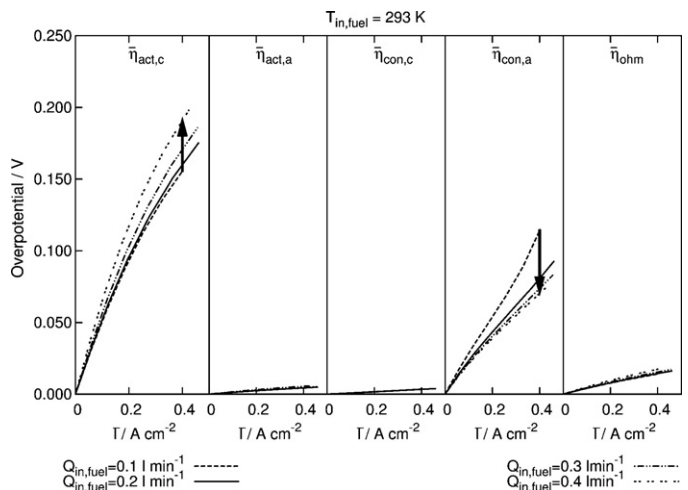**Fig. 9.** *I–V–P* curves for the cell given in Tables 1 and 2 at different fuel flow-rates.

Fig. 10. Mean overpotentials at different mean-current densities for the cell given in Tables 1 and 2 and for different fuel flow-rates.
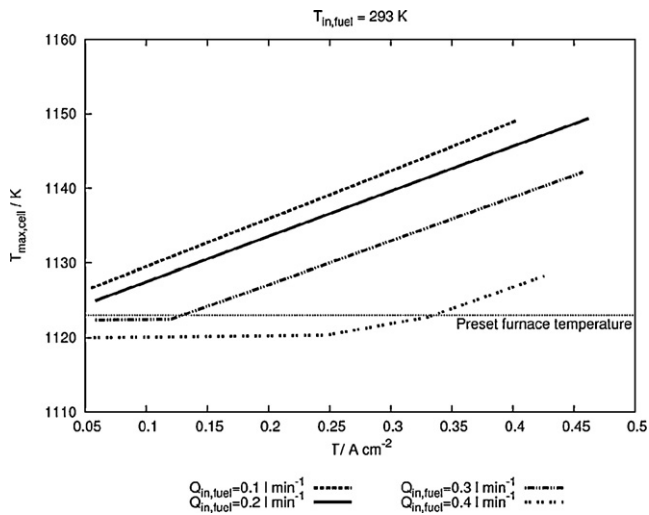
Fig. 11. Maximum cell temperature at different mean-current densities for the cell given in Tables 1 and 2 and for different fuel flow-rates.

the anode concentration-overpotential (as expected), but the activation overpotential is significantly increased due to a cooling effect shown in Fig. 11; this effect is often ignored in numerical simulations where the assumption $T_{in,fuel} = T_{oven}$ is made. Fig. 12 shows the temperature distribution inside the test rig when the cell is operating at 0.7 V without external fuel preheating for the three fuel inlet-velocities considered. As seen in Fig. 12, the fuel is heated as it flows inside the furnace from the inlet to the active area of the cell; at low fuel flow rates the fuel reaches the active-area at about the preset temperature as desired. However, at higher fuel-flow rates the path from the inlet to the active-area is not long enough for a full preheating of the gas. Fig. 11 also shows that the cell heat release even at high current densities may not be enough to heat the large non-preheated fuel flow. These results are also in agreement with the experimental curves reported by Suzuki et al. [4], who found a significant improvement of the cell performance when increasing the fuel inlet-velocity from 0.2 m s^{-1} to 0.4 m s^{-1} (873 K), but no major changes when further increasing it from 0.6 m s^{-1} to

0.8 m s^{-1}. It should be mentioned that the results by Suzuki et al. [4] at 823 K show however monotonic improvements in the cell performance with increasing the fuel flow-rate. This however does not contradict our findings regarding this cooling effect, since this effect becomes less relevant, or even negligible, at lower operating temperatures.

Thus the positive effect of the increased fuel flow on the concentration overpotential may be countered, depending on the fuel feeding-temperature, by the cooling effect of the flow. Among other corollaries, this highlights the importance of the precise knowledge of the operating/boundary conditions when respectively conducting and interpreting experiments/simulations. As an example, if $T_{in,fuel} = T_{oven}$ is improperly assumed, then the effects of the induced, and neglected, fuel-side cooling on the cell performance would be wrongly attributed to the electrochemistry parameters, which are often fitted from the results.

5. Conclusions

This paper has presented a comprehensive CFD model of the main mass and heat transfer processes taking place in a SOFC. The model uses five distinct but coupled subdomains for the two channels, the two electrodes and the electrolyte. An algorithm for coupling the solutions among these domains has been developed and presented.

The model has been validated by comparison with experimental results from a laboratory anode-supported tubular cell. Further, the model has been exploited to investigate the influence of the mass flow rates and thermal fields in the cell performance. It has been shown that, due to convective cooling, the cell performance may deteriorate for larger mass flow rates if the feeding temperature is low.
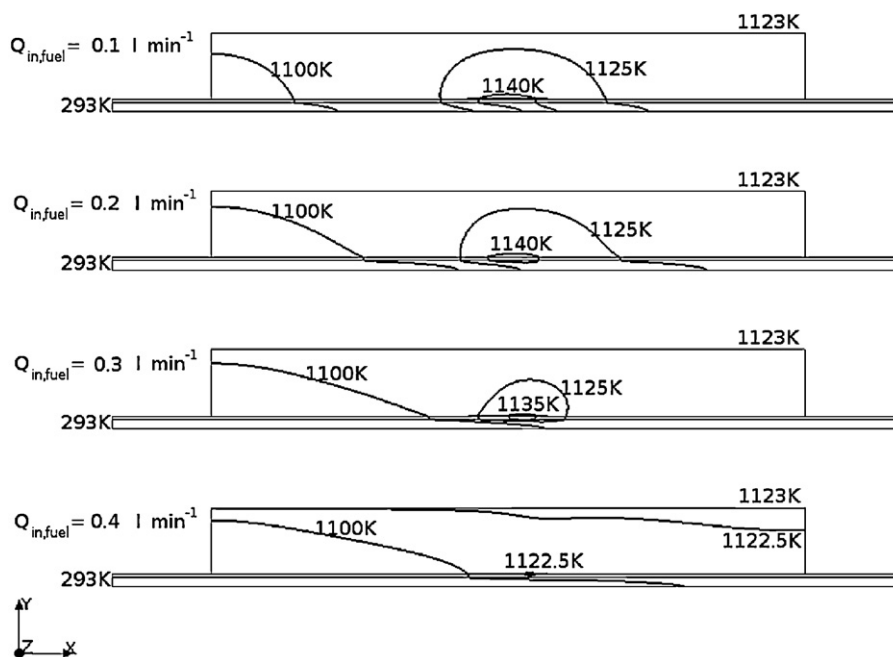
Acknowledgements

Fig. 12. Temperature contours (in Kelvin) for the cell given in Tables 1 and 2 at 0.7 V and different fuel flow-rates. The cell active area is indicated with a black straight line.

Table A1
Summary of surface-to-surface radiation in the air channel.

	Electrolyte	Cathode	Furnace wall	Furnace front-end	Furnace back-end
A_i	A_j	A_j	A_j	A_j	A_j
Electrolyte	×	×	√	√	√
Cathode	×	×	√	√	√
Furnace wall	√	√	√	√	√
Furnace front-end	√	√	√	×	√
Furnace back-end	√	√	√	√	×

Appendix A. Appendix

As indicated above, surface-to-surface radiation in the cell channels is the only radiation mechanism relevant in the operation of a solid-oxide cell. In the present model, the appropriate heat fluxes are calculated using a view-factor method, and inserted in the heat-transfer equations for the electrolyte and electrodes as boundary conditions at the electrode-channel and electrolyte-channel interfaces. This Appendix provides some additional details on the model implemented.

In the geometry analysed in this paper [5], the fuel channel consists of a long thin cylinder (2.4 mm diameter and 100 mm in length), made of a porous material (anode). The radiative heat flux at a given point of the fuel channel can thus arise only from irradiation from other locations at the anode surface. Considering: (i) axial symmetry; and (ii) view factors vanish quickly in the axial direction for such a thin cylinder; the surface-to-surface radiation in the fuel channel is neglected.

The air channel consists of the void space between the cylindrical furnace and the concentric cell. The cell external radius is 1.62 mm, in the non-reacting zone, and 1.67 mm where the cathode is printed (see Fig. 1). The furnace is 10 mm in radius. Both ends of the air channel are filled with a thermal-insulating porous-material, retaining the heat in the furnace while allowing the air go through. Surface-to-surface radiation thus takes place between several pairs of surfaces, as summarized in Table A1 and depicted in Fig. A1.

From the above discussion it is concluded, that there are five surfaces involved in the surface-to-surface thermal-radiation exchange: (i) the electrolyte external surface; (ii) the cathode external surface; (iii) the furnace heated wall; (iv) the furnace front-end; and (v) the furnace back-end. These are all included in the radiation model.

For calculating the radiative exchange among surfaces, these are discretized into a number of elementary surface elements. In this work, these elements are also the relevant faces of the computational mesh used for the finite-volume method. The radiative flux departing a surface element i, $q_{\mathrm{rad},i}$, is given by [22]:

$$q_{\mathrm{rad},i} = \varepsilon_{\mathrm{rad},i} \left\{ E_{\mathrm{b},i} - \sum_j (F_{i-j}E_{\mathrm{b},j}) - H_{\mathrm{o},i} \right.$$
$$\left. + \sum_j \left[\left(\frac{1}{\varepsilon_{\mathrm{rad},j}} - 1 \right) F_{i-j} q_{\mathrm{rad},j} \right] \right\} \tag{A1}$$

where the subindex j stands for each of the other surface elements that are viewed from element i; $\varepsilon_{\mathrm{rad}}$ is the emissivity of the surface, E_{b} is the blackbody emissive power, E_{o} is the incident radiation entering or leaving the enclosure through an opening, and F_{i-j} is the view factor between each two surface elements, A_i and A_j. The view factor is defined and calculated as:

$$F_{i-j} = \frac{\cos(\theta_i)\cos(\theta_j)}{\pi r^2} A_j = \frac{-(\vec{n}_i \cdot \vec{r})(\vec{n}_j \cdot \vec{r})}{\pi r^4} A_j \tag{A2}$$

where θ_i and θ_j are the angles between the surface normal vectors and the line connecting A_i and A_j (of length r), as shown in Fig. A1. This computation of view factors is performed only once, at the beginning of the calculation.

The radiative heat flux at each surface element is calculated as the solution of the system of equations given in Eq. (A1)

Regarding the emissivities of the different surfaces, the cell electrolyte is made of Yttria Stabilized Zirconia (YSZ), the emissivity of which is uncertain. Ferreire et al. [33] measured the YSZ emissivity at 1273 K, finding a value of 0.25; Alaruri et al. [34] calculated an effective emissivity of 0.4 for the YSZ samples without aluminium impurities at 1123 K; Sully et al. [35] measured the emissivity of the pure zirconia at 1073 K, obtaining a value around 0.32. The electrolyte emissivity is set to 0.4 in this work.
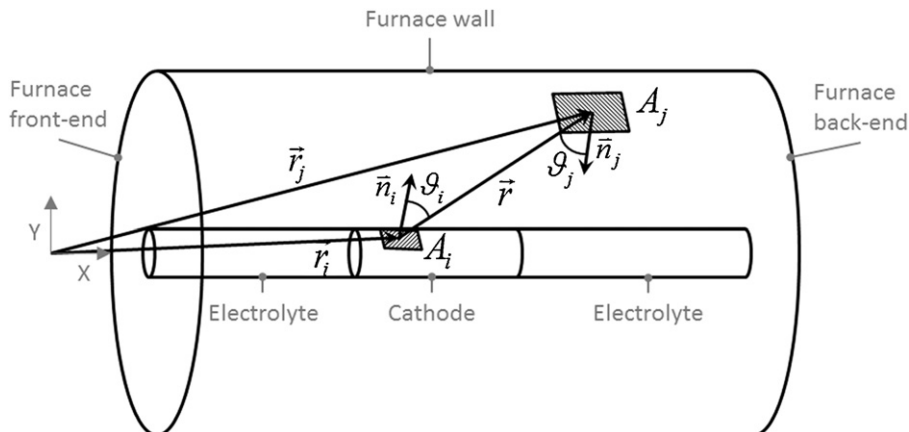

Fig. A1. Computational domain for view-factor calculation and surface-to-surface radiation model.

The cell cathode is made of a composite material, consisting of Lanthanum Strontium Manganite and Yttrium Stabilized Zirconia (LSM-YSZ). For a similar material, an emissivity of 0.4 has been reported [36], and is used in this model.

The material of the furnace enclosure is not known, and its emissivity is thus assumed to be 0.8.

References

[1] M.C. Williams, J. Strakey, W. Sudoval, Journal of Power Sources 159 (2) (2006) 1241–1247.
[2] M. Cali, M. Santarelli, P. Leone, Journal of Power Sources 156 (2) (2006) 400–413.
[3] N. Akhtar, S.P. Decent, K. Kendall, Numerical modelling of methane-powered micro-tubular, single-chamber solid-oxide fuel cell, Journal of Power Sources 195 (23) (2010) 7796–7807.
[4] T. Suzuki, Z. Hasan, Y. Funahashi, T. Yamaguchi, Y. Fujishiro, M. Awano, Science 325 (August (14)) (2009) 852–855.
[5] R. Campana, R.I. Merino, A. Larrea, I. Villarreal, V.M. Orera, Journal of Power Sources 192 (2009) 120–125.
[6] S. Hashimoto, H. Nishino, Y. Liu, K. Asano, M. Mori, Y. Funahashi, Y. Fujishiro, The electrochemical cell temperatura estimation of micro-tubular SOFCs during the power generation.
[7] M. García-Camprubí, A. Sánchez-Insa, N. Fueyo, Chemical Engineering Science 65 (5) (2010) 1668–1677.
[8] M. García-Camprubí, N. Fueyo. International Journal of Hydrogen Energy, Accepted.
[9] S. Kakaç, A. Pramuanjaroenkij, X.Y. Zhou, International Journal of Hydrogen Energy 32 (2007) 761–786.
[10] M. Andersson, J. Yuan, B. Sundèn, Applied Energy 87 (2010) 1461–1476.
[11] M. Désilets, P. Proulx, G. Soucy, International Journal of Heat and Mass Transfer 40 (18) (1997) 620–631.
[12] E. Mason, A. Malinauskas, Gas Transport in Porous Media: The Dusty-Gas Model, Elsevier, New York, 1983.
[13] C.R. Wilke, Chemical Engineering Progress 46 (1950) 95–104.
[14] R.H. Perry, D.W. Green, Perry's Chemical Engineers' Handbook, 7th Edition, McGraw-Hill International Editions, Chemical Engineering Series, 1998.
[15] J.O. Hirschfelder, C.F. Curtiss, R.B. Bird, Molecular Theory of Gases and Liquids, John Willey, 1954.
[16] F.M. White, Viscous Fluid Flow, McGrawHill, 1991.
[17] National Institute of Standards and Technology (NIST), www.nist.gov.
[18] S. Chapman, T.G. Cowling, The Mathematical Theory of Non-Uniform Gases, Third Edition, Cambridge University Press, Cambridge, 1970.
[19] F. Tong, L. Jing, R.W. Zimmerman, International Journal of Rock Mechanics & Mining Sciences 46 (2009) 1358–1369.
[20] D.L. Damm, A.G. Fedorov, Journal of Power Sources 143 (2005) 158–165.
[21] D. Sánchez, R. Chacartegui, A. Muñoz, T. Sánchez, Journal of Power Sources 160 (2006) 1074–1087.
[22] M.F. Modest, Radiative Heat Transfer, 2nd Edition, Academic Press, 2003.
[23] D.L. Damm, A.G. Fedorov, Journal of Power Sources 159 (2006) 1153–1157.
[24] K.J. Daun, S.B. Beale, F. Liu, G.J. Smallwood, Journal of Power Sources 157 (2006) 302–310.
[25] U.G. Bossel, Final Report on SOFC Data: Facts & Figures. International Energy Agency, Swiss Federal Office of Energy, Operating Agent Task II. Berne, April 1992.
[26] P. Costamagna, K. Honegger, Journal of the Electrochemical Society 185 (11) (1998) 3995–4006.
[27] S.V. Patankar, D.B. Spalding, International Journal of Heat and Mass Trasnfer 15 (10) (1972) 1787–1806.
[28] R. Campana, Pilas de Combustible de Óxido Sólido Microtubulares y Regenerativas en base YSZ o ScSZ de soporte anódico. Ph.D. thesis, Zaragoza, March 2010.
[29] M.F. Serincan, U. Pasaogullari, N.M. Sammes, Journal of Power Sources 192 (2009) 414–422.
[30] K. Oulmi, B. Zitouni, H.B. Moussa, H. Abdenebi, G.M. Andreadis, Total polarization effect on the location of maximum temperature value in planar SOFC, International Journal of Hydrogen Energy 36 (6) (2011) 4236–4243.
[31] D.H. Jeon, Electrochimica Acta 54 (2009) 2727–2736.
[32] Z. Qu, P.V. Aravind, S.Z. Boksteen, N.J.J. Dekker, A.H.H. Janssen, N. Woudstra. A.H.M. Verkooijen, inpress. Three-dimensional computational fluid dynamics modelling of anode-supported planar SOFC. International Journal of Hydrogen Energy.
[33] A. Ferriere, L. Lestrade, Journal of Solar Energy Engineering 122 (2000) 9–13.
[34] S.D. Alaruri, L. Bianchini, A.J. Brewington, Society of Photo-Optical Instrumentation Engineers 37 (2) (1998) 683–687.
[35] A.H. Sully, E.A. Brandes, R.B. Waterhouse, British Journal of Applied Physics 3 (1952) 97–102.
[36] J.-M. Klein, Y. Bultel, S. Georges, M. Pons, Chemical Engineering Science 62 (2007) 1636–1649.